Synchronous Switching and Control of WPT Systems With an Active Rectifier Based on Recursive Current Tracking

Fengwei Chen, Chanzhen Duan, Zhenxing Xu, Danli Chen, Lei Zhao, Jie Hou, and Udaya K. Madawala

***Abstract*—The control of wireless power transfer systems with an active rectifier can be implemented on the secondary side, which avoids the need for real-time wireless communication between the primary and secondary sides to construct the feedback loop, thus facilitating the control design. However, in secondary control we encounter the challenge of synchronous switching. In this article, a data-based approach is proposed to address this challenge, which first applies a recursive algorithm to estimate in real time the amplitude and phase of the input current of the active rectifier from sampled data, then generates the driving signals based on the estimated phase for the active rectifier to control the relative phase angle between the input voltage and current of the active rectifier, and finally performs secondary phase-shift control to regulate the load power. The recursive algorithm for current tracking has the merits of relying on data only, so it requires less peripheral circuit components, and shows high accuracy in current phase detection and synchronous switching because the current parameters are optimized in a minimal prediction error sense. Moreover, it also shows good tracking ability under conditions, such as system detuning, harmonic distortion, primary–secondary frequency mismatch, etc. At the same time, it has a moderate computational burden, each recursion consuming about 416 clock periods when implemented on the 200-MHz digital signal processor TMS320F28377D. To facilitate control design, a low-order model is identified from sampled data to characterize the dominant dynamic behavior of the system and, then, used to tune the proportional–integral–derivative control parameters. The effectiveness of the proposed control method is validated on a 1.5-kW level prototype.**

***Index Terms*—Active rectifier, fundamental tracking, secondary-side control, wireless power transfer (WPT).**

Received 10 April 2025; revised 8 July 2025; accepted 27 July 2025. Date of publication 5 August 2025; date of current version 22 October 2025. This work was supported by the National Natural Science Foundation of China under Grant 62073246, Grant 52207002, and Grant 62373070. Recommended for publication by Associate Editor S. Y. Jeong. *(Corresponding author: Lei Zhao.)*

Fengwei Chen, Chanzhen Duan, Zhenxing Xu, Danli Chen, and Lei Zhao are with the School of Automation, Chongqing University, Chongqing 400044, China (e-mail: fengwei.chen@cqu.edu.cn; duancz@stu.cqu.edu.cn; 202313131120@stu.cqu.edu.cn; chendanli@stu.cqu.edu.cn; lzha915@cqu.edu.cn).

Jie Hou is with the College of Automation, Chongqing University of Posts and Telecommunications, Chongqing 400065, China (e-mail: houjie@cqupt.edu.cn).

Udaya K. Madawala is with the Department of Electrical and Computer Engineering, The University of Auckland, Auckland 1010, New Zealand (e-mail: u.madawala@auckland.ac.nz).

Color versions of one or more figures in this article are available at https://doi.org/10.1109/TPEL.2025.3596013.

Digital Object Identifier 10.1109/TPEL.2025.3596013

I. Introduction

WIRELESS power transfer (WPT) has received widespread attention due to its physical isolation characteristics that enable power transmission without contact, effectively improving the safety, reliability, and flexibility of power supply [1], [2], [3], [4]. The WPT technology has been widely applied in consumer electronics [5], [6], electric vehicles [7], [8], underwater equipment [9], [10], biomedical [11], [12], and other fields [13], [14]. Closed-loop control is a common approach to improve the performance of power electronic systems [15], [16], [17]. Existing control methods for WPT systems can be divided into two categories: primary-side control [17], [18] and secondary-side control [19], [20]. Primary-side control has been widely investigated due to its simplicity, but in WPT systems it requires wireless communication to exchange data between the primary and secondary sides, where issues such as communication delay and package losses will impair the feedback performance [18]. Secondary-side control replaces the diode bridge by an active bridge and uses active rectification to regulate the load power on the secondary side, which avoids the problems encountered in primary-side control, thus improving the control system performance. Therefore, this article focuses on the secondary-side control scheme.

A prerequisite for the secondary-side control is to align the input voltage and current of the rectifier in opposite phase. If this is not satisfied, reactive power will circulate in the system, which may reduce system efficiency, or even cause instability problems [19], [20], [21], [22], [23]. This issue is also called synchronization in bidirectional WPT systems, where the aim is to adjust the relative phase angle between the inverter output voltage and rectifier input voltage and the available methods are categorized as follows. 1) Introducing an additional communication link to transmit the primary-side phase information to the secondary side [24], [25], [26]. However, in practical applications, complete decoupling between the auxiliary coil and the power transfer coils is sometimes difficult to achieve, which may result in reduced synchronization accuracy. A pulse synchronization scheme based on wireless power and data simultaneous transmission technology is proposed in [27], where a phase lock technique is introduced to mitigate the false triggering problem originating from the interference of the power channel on the data channel. 2) Directly detecting the phase of the rectifier input current and aligning it with the rectifier

input voltage [28], [29], [30]. As such, the relative phase angle between the voltages generated by the inverter and rectifier is adjusted to the desired value. In [29] and [30], the phase of the rectifier input current is determined via zero-crossing detection. This method has the merit of fast response and ease of implementation, but it requires a filtering circuit to attenuate the harmonics and measurement noise in the rectifier input current, which inevitably introduces time delays and inaccuracy. In [31] and [32], the synchronization angle is solved as the inverse tangent function constructed from the active and reactive power flowing through the active rectifier. This method is less sensitive to harmonics and measurement noise, but the hardware implementation could be more complicated. In [33], a fully digital synchronization method is proposed, which performs active and reactive current decomposition based on sampled resonant current data to accurately extract the phase difference between the fundamental components of rectifier input voltage and current, achieving higher accuracy. However, this method requires high sampling rate and field programmable gate array for high-speed digital signal processing, which significantly increases the hardware complexity and computational burden. Similarly, in [27] and [34], an in-phase/quadrature detection method, which utilizes a multiplexer-based phase detection circuit to generate a pair of orthogonal virtual five-level piecewise constant signals, is developed for phase synchronization. This approach not only eliminates influence of harmonic distortions but also avoids the use of analog multipliers or complex digital signal processing. As a result, it achieves fast transient response while maintaining low phase-locking error.

In [35], a lock-in amplifier is used to convert the voltage vector into a sinusoidal signal without harmonics which, together with a compensation technique to address the delays caused by signal processing, achieves better synchronization performance. In [36], considering the variation of the operating point parameters, the transfer function between the controlled output and the phase detector in the phase synchronization loop is derived, and the phase synchronization controller is designed to ensure the stability of the system within a wide range of operating point parameters. In [37], by introducing an equivalent sensor inductor (a magnetic ring with multiturn wires) in series with the resonant network on the secondary side, sudden changes in the output voltage of the inverter can cause voltage transients in the sensor inductor. Through the detection and tracking of the voltage transient process, frequency and phase synchronization on both sides can be achieved. In [38], a pulse voltage injection method is proposed. Voltage pulses are injected on the primary side and detected on the secondary side to generate synchronous signals. By capturing the synchronization signal, the frequency and phase of the primary side can be locked. Although this method has high accuracy and a fast response speed, it is greatly affected by the disturbance on the resonant current. Furthermore, when the transmission power increases, the total cost of the system will also rise.

One of the objectives of this article is to develop a robust method to detect the phase of the rectifier input current in real time. The developed method performs the following: first, the rectifier input current is sampled at a rate that is sufficient to recover its fundamental from sampled data; then, a recursive algorithm is applied to estimate the amplitude and initial phase of the fundamental from the sampled data; finally, based on the estimated initial phase, the voltage of the active rectifier is generated to realize active rectification. For closed-loop control of the load voltage, it would be more efficient if a model of the system is established and then used to help tune the control parameters. Traditional modeling methods for WPT systems include the generalized state space averaging method [41], the extended describing function method [42], and the ac impedance analysis method [43], etc. These methods normally require to know the system topology and circuit component parameters, and they always result in complex models which cannot be directly used for control design. As an alternative, this article adopts the system identification (or data-driven modeling) method to build simple yet accurate models, which are more preferred for control system design [44], [45], [46], [47]. In primary-side phase-shift (PS) control, the Hammerstein model, composed of a static input nonlinearity function followed by a linear transfer model, has been used not only to describe the dynamic behavior of a WPT system, but also to describe the static nonlinearity of the inverter. After compensating for the static input nonlinearity, the system can be viewed as a linear system and linear control design methods can be applied [18]. In this article, a Hammerstein model will be established for WPT systems with secondary-side PS control, and further used to tune the proportional–integral–derivative (PID) controller. The contributions of this article are as follows.

1) A recursive algorithm is proposed to track the fundamental of the rectifier input current. Since the recursive algorithm finds out the optimal parameters by minimizing a quadratic cost function constructed from the historical data, enhanced robustness against harmonic distortions can be achieved. Moreover, the proposed method can directly handle the case where both the amplitude and phase of the rectifier input current are time varying, which occurs when the primary and secondary clock frequencies are not completely the same, or when the system is in a transient state.
2) A Hammerstein model is used to describe the dynamic behavior of a WPT system with secondary-side PS control. The parameters of the Hammerstein model are estimated using a system identification method from the sampled PS angle and load voltage data. Then, a PID controller is designed based on the identified Hammerstein model. The proposed methodology is a general procedure that improves the efficiency of control design for WPT systems.

The rest of this article is organized as follows. In Section II, a recursive tracking algorithm is presented and the synchronous switching control of the active rectifier is discussed. In Section III, the proposed method is compared with an existing method to show its superiority. In Section IV, a data-driven modeling method is used to build a Hammerstein model for the system, and a PID controller is designed based on this model. Sections V and VI present experimental results to demonstrate the effectiveness of the proposed method. Finally, Section VII concludes this article.

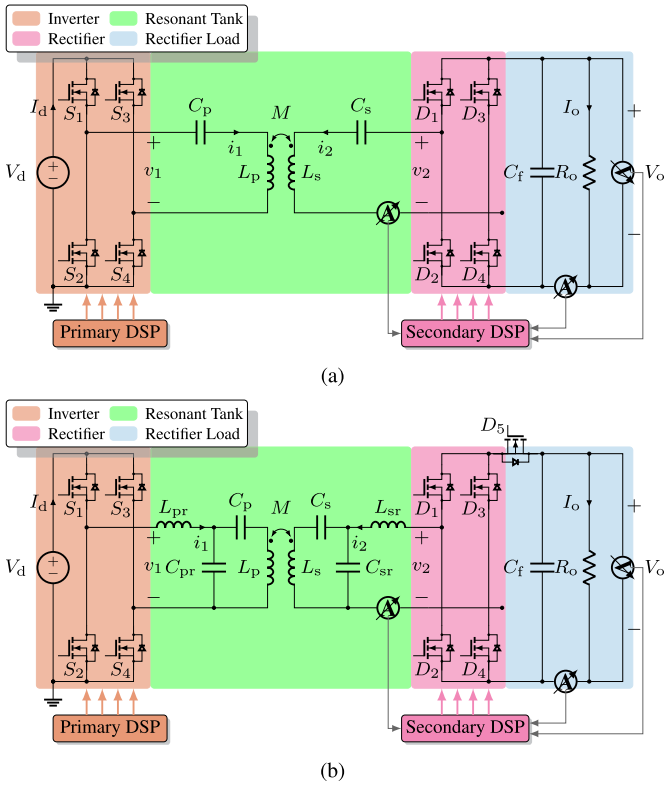

Fig. 1. Circuit topologies. (a) SS WPT system with an active rectifier. (b) LCC–LCC WPT system with an active rectifier.

II. Recursive Current Parameter Tracking

A. System Description

In this section, we begin with a series–series (SS) WPT system with an active rectifier sketched in Fig. 1(a). Note that the method proposed in this article can be directly applied to other topologies, such as the LCC–LCC topology shown in Fig. 1(b). The dc voltage V_d is converted to the ac voltage v_1 through a full-bridge inverter composed of S_1–S_4 and then fed to the resonant tank. Since the coils L_p and L_s are loosely coupled with mutual inductance M being small, appropriate compensation is required on both sides to compensate for the leakage inductance. After that, the ac current i_2 induced in the secondary coil is converted to the dc load current I_o through the active rectifier composed of D_1–D_4 and output capacitor C_f. Note that a switch is cascaded to the rectifier bridge to block reactive power flowing through the rectifier bridge.

The load voltage V_o or current I_o of the system is regulated by the active rectifier on the secondary side, so the control variables are chosen as σ, which is the PS between two legs of the active rectifier, and δ, which is the relative phase angle between the rectifier input voltage v_2 and current i_2 (see Fig. 2 for the definitions of σ and δ). Under the assumption of first harmonic approximation, the phasors of v_2 and i_2 are expressed as

$$\dot{V}_2 = V_2 \mathrm{e}^{j\omega t}, \quad \dot{I}_2 = I_2 \mathrm{e}^{j(\omega t-\delta)} \tag{1}$$

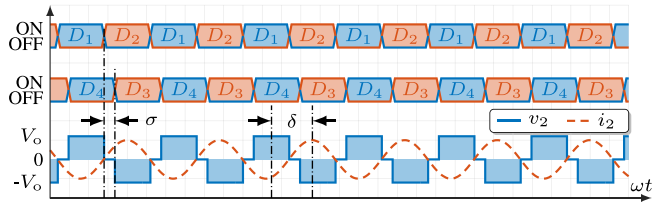

Fig. 2. Waveform in the active rectifier.

where ω is the angular switching frequency; the capital letters V_2 and I_2 denote the amplitudes of v_2 and i_2, respectively. Moreover

$$v_2 \approx \mathrm{Re}\{\dot{V}_2\} = V_2 \cos(\omega t) \tag{2a}$$

$$i_2 \approx \mathrm{Re}\{\dot{I}_2\} = I_2 \cos(\omega t - \delta). \tag{2b}$$

Since v_2 is a square wave, it can be shown that

$$V_2 = \frac{4}{\pi} V_\mathrm{o} \cos(\sigma/2). \tag{3}$$

By the law of energy conservation, the relationship between I_2 and I_o is established as

$$\begin{aligned} V_\mathrm{o} I_\mathrm{o} &= -\frac{1}{T_0}\int_0^{T_0} v_2 i_2 dt \\ &= -\frac{1}{T_0}\int_0^{T_0} V_2 I_2 \cos(\omega t)\cos(\omega t-\delta) dt \\ &= -\frac{1}{2} V_2 I_2 \cos(\delta) \end{aligned} \tag{4}$$

where T_0 is switching period. Substitution of (3) into (4) yields

$$I_\mathrm{o} = -\frac{2}{\pi} I_2 \cos(\sigma/2)\cos(\delta). \tag{5}$$

Then, based on (1)–(5), the ac equivalent impedance of the rectifier Z_eq is derived as

$$\begin{aligned} Z_\mathrm{eq} &= \frac{\dot{V}_2}{\dot{I}_2} = \frac{V_2}{I_2}\mathrm{e}^{j\delta} \\ &= -\frac{4}{\pi} V_\mathrm{o} \cos(\sigma/2) \cdot \frac{2}{\pi I_\mathrm{o}} \cos(\sigma/2)\cos(\delta)\mathrm{e}^{j\delta} \\ &= -\frac{8}{\pi^2} R_\mathrm{o} \cos^2(\sigma/2)\cos(\delta)\mathrm{e}^{j\delta}. \end{aligned} \tag{6}$$

If $\delta = \pi - \sigma/2$ rad, the rectifier will be operated in the zero voltage switching (ZVS) state

$$Z_\mathrm{eq} = -\frac{8}{\pi^2} R_\mathrm{o} \cos^3(\sigma/2)\mathrm{e}^{-j\sigma/2} \tag{7a}$$

$$I_\mathrm{r} = I_\mathrm{o} = \frac{2}{\pi} I_2 \cos^2(\sigma/2) \tag{7b}$$

where I_r is the average rectified current, while when $\delta = \pi$ rad, the rectifier will be operated in the zero-phase angle (ZPA) state

$$Z_\mathrm{eq} = -\frac{8}{\pi^2} R_\mathrm{o} \cos^2(\sigma/2) \tag{8a}$$

$$I_\mathrm{r} = I_\mathrm{o} = \frac{2}{\pi} I_2 \cos(\sigma/2) \tag{8b}$$

where it can be seen that $Z_{\rm eq}$ is purely resistive. In the rest of this section, it is assumed that the system is operated at the ZPA state. It is further assumed that the primary and secondary resonators have the same frequency, i.e., $\omega^2 = 1/(L_{\rm p}C_{\rm p}) = 1/(L_{\rm s}C_{\rm s})$. When the equivalent series resistances of coils are negligible and the switches and diodes are considered as ideal, we have

$$Z_{\rm p}(j\omega) = j\omega L_{\rm p} + \frac{1}{j\omega C_{\rm p}} = 0 \tag{9a}$$

$$Z_{\rm s}(j\omega) = j\omega L_{\rm s} + \frac{1}{j\omega C_{\rm s}} + R_{\rm eq} = R_{\rm eq} \tag{9b}$$

in which we have used $R_{\rm eq}$ instead of $Z_{\rm eq}$ to emphasize that the equivalent impedance is resistive. Under the above-mentioned assumptions, according to Kirchoff's voltage law, we have

$$Z_{\rm p}(j\omega)\dot{I}_1 + j\omega M\dot{I}_2 = \dot{V}_1 \tag{10a}$$

$$Z_{\rm s}(j\omega)\dot{I}_2 + j\omega M\dot{I}_1 = 0 \tag{10b}$$

from which $\dot{I}_2$ can be solved as

$$\dot{I}_2 = -\frac{j\omega M}{Z_{\rm p}(j\omega)Z_{\rm s}(j\omega) + \omega^2 M^2}\dot{V}_1 = \frac{1}{j\omega M}\dot{V}_1. \tag{11}$$

The result in (11) indicates that $\dot{I}_2$ is decoupled with the load, and so the system behaves like a current source. This property will be used in Section IV-A to derive the model structure used for dynamic modeling and control design of the system.

B. Fundamental Current Tracking

The input current of rectifier i_2 can be written as the sum of harmonics via Fourier series expansion as follows:

$$i_2 = \sum_{n=1}^{\infty} a_n \sin\left(n\omega t + \tau_n\right) \tag{12}$$

where a_n and τ_n are the amplitude and initial phase of the nth harmonic, respectively. Since the resonant network is highly frequency selective, it is reasonable to perform the following fundamental approximation:

$$i_2 \approx a\sin\left(\omega t + \tau\right). \tag{13}$$

It is assumed that ω is known a priori, while the amplitude a and initial phase angle τ are unknown parameters to be estimated. Letting $\theta = [a, \tau]^{\rm T}$ be the vector of parameters of the fundamental, we propose to estimate θ in real time from the sampled data $\{i^*_{2,\ell}\}_{\ell=1}^{k}$, where $(\cdot)^*$ denote the sampled version of $(\cdot)$ and the subscript ℓ is the time index of sample. The parameter estimation problem is defined as

$$\widehat{\theta} = \arg\min_{\theta} \frac{1}{2} J_k(\theta) \tag{14a}$$

$$J_k(\theta) = \arg\min_{\theta} \sum_{\ell=1}^{k} \left(i^*_{2,\ell} - i_{2,\ell}\right)^2. \tag{14b}$$

The Gauss–Newton (GN) method can be used to solve the above-mentioned problem [45], [46]. Define the gradient $\nabla J_k(\theta)$ and Hessian matrix $\nabla^2 J_k(\theta)$ as

$$\nabla J_k(\theta) = -\sum_{\ell=1}^{k} \phi_\ell(\theta)\left(i^*_{2,\ell} - i_{2,\ell}\right) \tag{15a}$$

$$\nabla^2 J_k(\theta) = \sum_{\ell=1}^{k} \phi_\ell(\theta)\phi_\ell^{\rm T}(\theta) \tag{15b}$$

where

$$\begin{aligned}\phi_\ell^{\rm T}(\theta) &= \left[\frac{\partial i_2}{\partial a} \quad \frac{\partial i_2}{\partial \tau}\right]\Big|_{t=t_\ell} \\ &= \left[\sin\left(\omega t_\ell + \tau\right) \quad a\cos\left(\omega t_\ell + \tau\right)\right].\end{aligned} \tag{16}$$

Since the cost function $J_k(\theta)$ is nonlinear in θ, it should be linearized as follows before proceeding to the parameter estimation stage:

$$\begin{aligned}J_k(\theta) \approx\ & J_k(\widehat{\theta}_{k-1}) + \nabla J_k(\widehat{\theta}_{k-1})(\theta - \widehat{\theta}_{k-1}) \\ & + \frac{1}{2}(\theta - \widehat{\theta}_{k-1})^{\rm T}\nabla^2 J_k(\widehat{\theta}_{k-1})(\theta - \widehat{\theta}_{k-1})\end{aligned} \tag{17}$$

where $\widehat{\theta}_{k-1}$ is an estimate of θ that minimizes $J_{k-1}(\theta)$ obtained at the $(k-1)$th instant. Then, the solution that minimizes $J_k(\theta)$ is obtained as

$$\widehat{\theta}_k = \widehat{\theta}_{k-1} - \left[\nabla^2 J_k(\widehat{\theta}_{k-1})\right]^{-1}\nabla J_k(\widehat{\theta}_{k-1}). \tag{18}$$

Note that (18) is in a batch form, where the historical data up to the kth instant are used to update the parameter vector, which leads to high computational burden and large data storage each time a new estimate of θ is required. To avoid this problem, we further derive a recursive version of (18) which do not need to record historical data and is more computationally efficient. Letting $P_k^{-1} = \nabla^2 J_k(\widehat{\theta}_{k-1})$, it is direct that

$$P_k^{-1} = P_{k-1}^{-1} + \widehat{\phi}_k\widehat{\phi}_k^{\rm T} \tag{19}$$

where $\widehat{\phi}_k = \phi_k(\widehat{\theta}_{k-1})$.

Lemma 1: Let A, B, C, and D be matrices of appropriate dimension. If A and C are invertible, then

$$(A + BCD)^{-1} = A^{-1} - A^{-1}B\left(DA^{-1}B + C^{-1}\right)DA^{-1}. \tag{20}$$

Applying Lemma 1 to (19), we obtain

$$\begin{aligned}P_k &= \left(P_{k-1}^{-1} + \widehat{\phi}_k\widehat{\phi}_k^{\rm T}\right)^{-1} \\ &= P_{k-1} - \underbrace{\frac{P_{k-1}\widehat{\phi}_k}{1 + \widehat{\phi}_k^{\rm T}P_{k-1}\widehat{\phi}_k}}_{L_k}\widehat{\phi}_k^{\rm T}P_{k-1} \\ &= P_{k-1} - L_k\widehat{\phi}_k^{\rm T}P_{k-1}.\end{aligned} \tag{21}$$

Since $\widehat{\theta}_{k-1}$ minimizes $J_{k-1}(\theta)$, i.e., $\nabla J_{k-1}(\widehat{\theta}_{k-1}) = 0$, then (15a) becomes

$$\nabla J_k(\widehat{\theta}_{k-1}) = \nabla J_{k-1}(\widehat{\theta}_{k-1}) - \widehat{\phi}_k\widehat{e}_k = -\widehat{\phi}_k\widehat{e}_k \tag{22}$$

where $\widehat{e}_k = i^*_{2,k} - \widehat{i}_{2,k}$ and $\widehat{i}_{2,k}$ is a prediction of i_2 generated by using $\widehat{\theta}_{k-1}$. Substituting (21) and (22) into (18) yields

$$\begin{aligned}\widehat{\theta}_k &= \widehat{\theta}_{k-1} + P_k\widehat{\phi}_k\widehat{e}_k \\ &= \widehat{\theta}_{k-1} + \left(P_{k-1}\widehat{\phi}_k - L_k\widehat{\phi}_k^{\mathrm{T}}P_{k-1}\widehat{\phi}_k\right)\widehat{e}_k \\ &= \widehat{\theta}_{k-1} + L_k\widehat{e}_k. \end{aligned} \tag{23}$$

The equations in (21) and (23) form the recursive GN algorithm for the estimation of θ. However, this algorithm may have poor tracking performance if θ is time varying. To improve the tracking performance for time-varying parameters, the forgetting factor algorithm can be employed, leading to the following algorithm:

$$L_k = \frac{P_{k-1}\widehat{\phi}_k}{\lambda + \widehat{\phi}_k^{\mathrm{T}}P_{k-1}\widehat{\phi}_k} \tag{24a}$$

$$\widehat{\theta}_k = \widehat{\theta}_{k-1} + L_k\widehat{e}_k \tag{24b}$$

$$P_k = \frac{1}{\lambda}\left(P_{k-1} - L_k\widehat{\phi}_k^{\mathrm{T}}P_{k-1}\right) \tag{24c}$$

where $\lambda \leqslant 1$ is the forgetting factor.

Some algorithmic issues are discussed in the following remark.

Remark 1: The initial value for P can be selected as $P_0 = \epsilon I$, where I is an identity matrix of appropriate dimension and ϵ is a sufficiently large number, while $\widehat{\theta}_0$ can be set as a very small value. It should be aware that when $i^*_{2,k}$ is corrupted by measurement noise, since the partial derivative $\phi_k(\theta)$ defined in (16) is statistically independent of measurement noise, it can be inferred that the gradient $\nabla J_k(\theta)$ will not be affected by measurement noise and, so, the resulting parameter estimates are unbiased. As regards the sampling frequency, the Shannon sampling theorem shows that the sampling frequency must be at least twice higher than the target frequency. While a faster sampling rate can enhance parameter estimation accuracy, it is also important to consider the computational burden of the algorithm. Here, we suggest to set the sampling frequency to be three or four times the switching frequency to tradeoff between computational burden and tracking performance.

Remark 2: In real applications, the secondary controller can always not generate the same frequency as the primary controller, due to reasons such as manufacture errors in crystal oscillators. In this case, by reformulating the phase of i_2 as

$$\psi = (\omega_{\mathrm{s}} + \Delta\omega)\,t + \tau = \omega_{\mathrm{s}}t + (\Delta\omega t + \tau) \tag{25}$$

where ω_{s} is the actual frequency generated by the secondary controller, while $\Delta\omega$ is the bias, it can be seen that $\Delta\omega$ is now absorbed to form a time-varying initial phase $\Delta\omega t + \tau$. Fortunately, the proposed recursive algorithm (24) is able to track this time-varying parameter, thanks to the use of the forgetting algorithm. Moreover, by adjusting the values of the forgetting factor λ, we can balance between the stability and speed in the tracking process.

Remark 3: In order to improve the tracking accuracy of when $\tau\Delta\Omega t$, in (25) is not zero we can add an integration in (24) to capture this error term as follows:

$$\widehat{\mu}_k = \widehat{\mu}_{k-1} + \gamma\Delta\widehat{\theta}_k(2) \tag{26a}$$

$$\widehat{\theta}_k(2) = \widehat{\theta}_{k-1}(2) + \Delta\widehat{\theta}_k(2) + \widehat{\mu}_k \tag{26b}$$

where γ is the integration coefficient, $\widehat{\theta}_k(2)$ denotes the second entry of $\widehat{\theta}_k$, and $\Delta\theta_k = L_k\widehat{e}_k$.

TABLE I
CONFIGURATION REGISTERS OF A PWM MODULE

Symbol	Explanation	Expression
n_{prd}	Period the PWM counter	round $(2\pi/(\omega T_{\mathrm{clk}}))^{\dagger}$
n_{cnt}	Counter value	mod (round (t/T_{clk}), n_{prd})
n_{ip}	Initial phase of i_2	round $(\tau/\Lambda)^{\ddagger}$
n_{ps}	PS	round (σ/Λ)
n_{cmpa}	Instant to switch off D_2	$n_{\mathrm{prd}} - n_{\mathrm{ip}}$
n_{cmpb}	Instant to switch on D_2	$n_{\mathrm{cmpa}} \pm n_{\mathrm{prd}}/2$

$^{\dagger}T_{\mathrm{clk}}$ is the clock period of the DSP
$^{\ddagger}\Lambda = 2\pi/n_{\mathrm{prd}}$

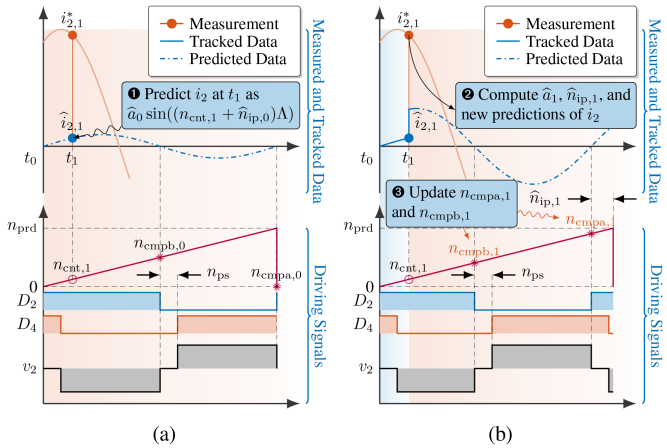

Fig. 3. Implementation of the proposed algorithm in the first recursion. (a) Predict $\widehat{i}_{2,1}$ based on the initial parameters $\widehat{a}_0$ and $\widehat{n}_{\mathrm{ip},0}$ (here $\widehat{n}_{\mathrm{ip},0} = 0$ is assumed). (b) Update $\widehat{a}_1$ and $\widehat{n}_{\mathrm{ip},1}$ using the measurement $i^*_{2,1}$, and then compute the new predictions of i_2, as well as the counter-compare registers $n_{\mathrm{cmpa},1}$ and $n_{\mathrm{cmpb},1}$. $n_{\mathrm{cmpa},k}$, $n_{\mathrm{cmpb},k}$, $n_{\mathrm{cnt},k}$, and $n_{\mathrm{ip},k}$ denote the register values obtained at time instant t_k.

C. Implementation in Digital Signal Processors (DSPs)

In DSPs, the timing of a control procedure is normally provided by a pulsewidth modulation (PWM) module. Therefore, the phase of (13) should be reformulated in terms of the configuration registers of a PWM module listed in Table I, where ZVS operation is configured, before the proposed recursive algorithm, as well as the synchronous switching control to be introduced later, can be implemented. With these notations, (13) can be rewritten as

$$i_2 = a\sin\left[(n_{\mathrm{cnt}} + n_{\mathrm{ip}})\,\Lambda\right] \tag{27}$$

where, for the sake of clarity, it is imposed that $n_{\mathrm{cnt}} \in [0, n_{\mathrm{prd}})$ and $n_{\mathrm{ip}} \in (0, n_{\mathrm{prd}}]$.

The variables listed in Table I are also annotated in Fig. 3. When $n_{\rm ip}$ is available, in the following we explain how to configure the counter-compare registers of the PWM module to generate the driving signals for D_1 to D_4. Note that only the driving signals for D_2 and D_4 are shown in Fig. 3, because the driving signal for D_1 (D_3) is complementary to that of D_2 (D_4). The driving signal for D_2 has the same sign than i_2. Since the phase of i_2 is $n_{\rm cnt}+n_{\rm ip}$, and $n_{\rm ip}\in(0,n_{\rm prd}]$ as imposed in (27), it is clear that D_2 should be switched ON when $n_{\rm cnt}+n_{\rm ip}=n_{\rm prd}$, or OFF when $n_{\rm cnt}+n_{\rm ip}=n_{\rm prd}\pm n_{\rm prd}/2$. Here, we use two counter-compare registers A and B to trigger the ON and OFF states of D_2, respectively. Under the ZVS operation, the values for the two registers are computed as

$$n_{\rm cmpa}=n_{\rm prd}-n_{\rm ip} \tag{28a}$$

$$n_{\rm cmpb}=\begin{cases} n_{\rm cmpa}+n_{\rm prd}/2 & \text{if } n_{\rm cmpa}<n_{\rm prd}/2 \\ n_{\rm cmpa}-n_{\rm prd}/2 & \text{otherwise.}\end{cases} \tag{28b}$$

By taking into account the PS $n_{\rm ps}$, the driving signals for D_4 can be generated in a similar way using another two counter-compare registers $n_{\rm cmpc}$ and $n_{\rm cmpd}$

$$n_{\rm cmpc}={\rm rem}(n_{\rm cmpa}+n_{\rm ps},n_{\rm prd}) \tag{29a}$$

$$n_{\rm cmpd}=\begin{cases} n_{\rm cmpc}+n_{\rm prd}/2 & \text{if } n_{\rm cmpc}<n_{\rm prd}/2 \\ n_{\rm cmpc}-n_{\rm prd}/2 & \text{otherwise}\end{cases} \tag{29b}$$

where rem is the remainder operator. The main steps in each recursion are summarized in the following.

- Prediction: At some time instant, for example t_1, compute the prediction of i_2 (denoted by $\widehat{i}_{2,1}$) by using the parameters at time instant t_0, denoted by $\widehat{a}_0$ and $\widehat{n}_{{\rm ip},0}$, as
$$\widehat{i}_{2,1}=\widehat{a}_0\sin\left[(n_{{\rm cnt},1}+\widehat{n}_{{\rm ip},0})\,\Lambda\right]. \tag{30}$$
It is possible to generate the prediction of i_2 at any future instant in the same way; see the dash dot line in Fig. 3.
- Correction: When a measurement $i^*_{2,1}$ becomes available at time instant t_1, we update the parameters $\widehat{a}_1$ and $\widehat{n}_{{\rm ip},1}$ according to (24) using the innovation $i^*_{2,1}-\widehat{i}_{2,1}$. At the same time, the counter-compare register values $n_{{\rm cmpa},1}$ and $n_{{\rm cmpb},1}$ are also updated based on $\widehat{n}_{{\rm ip},1}$ according to (28).

By repeating the above-mentioned two steps, recursive tracking of i_2 and synchronous switching control can be achieved; see Fig. 4 for a snapshot of the initial ten recursions of the tracking process. In Fig. 4, the counter-compare register values are updated immediately when new parameter estimates become available. Optionally, one can choose to update these registers only once per PWM period at a certain instant, such as the time when reloading the counter. Finally, the proposed recursive tracking and synchronous control (RTSC) algorithm is summarized as Algorithm 1.

III. Comparison With Existing Method

In this section, the proposed RTSC method is compared with the active and reactive current decomposing (ARCD) method [33] to show its merits. Fig. 5 shows the schematic

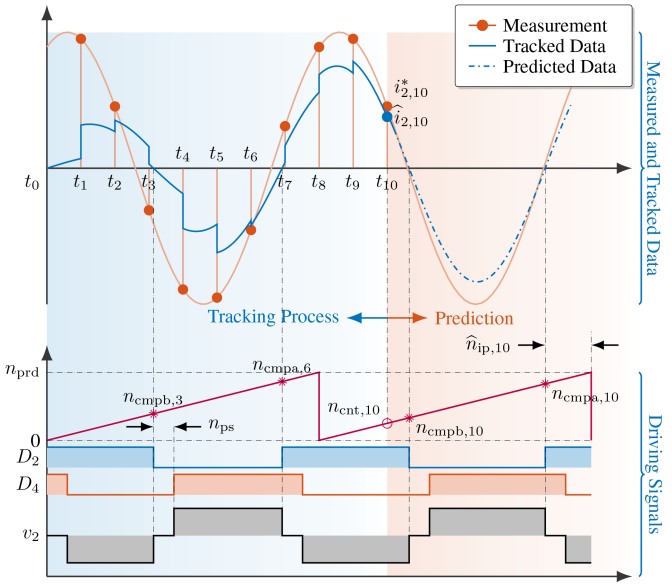

Fig. 4. Tracking and synchronous control in two PWM cycles.

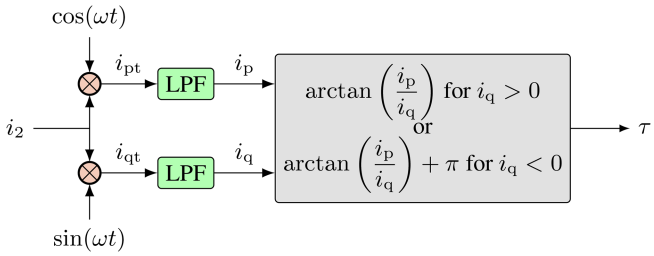

Fig. 5. Schematic diagram of active and reactive current decomposition method.

diagram of the ARCD method. Since $i_2=a\sin(\omega t+\tau)$, the intermediate signals $i_{\rm pt}$ and $i_{\rm qt}$ are then computed as

$$i_{\rm pt}=i_2\cos(\omega t)=\frac{a}{2}\left[\sin(\tau)+\sin(2\omega t+\tau)\right] \tag{31a}$$

$$i_{\rm qt}=i_2\sin(\omega t)=\frac{a}{2}\left[\cos(\tau)-\cos(2\omega t+\tau)\right] \tag{31b}$$

where it can be seen that each signal is composed of a dc term plus or minus an ac term. By passing these through a low-pass filter (LPF), then the ac term is filtered out, and we obtain

$$i_{\rm p}=\frac{a}{2}\sin(\tau),\quad i_{\rm q}=\frac{a}{2}\cos(\tau) \tag{32}$$

from which a and τ can be obtained as

$$\widehat{a}=2\sqrt{i_{\rm p}^2+i_{\rm q}^2} \tag{33a}$$

$$\widehat{\tau}=\begin{cases}\arctan\left(i_{\rm p}/i_{\rm q}\right) & i_{\rm q}>0 \\ \arctan\left(i_{\rm p}/i_{\rm q}\right)+\pi & i_{\rm q}<0.\end{cases} \tag{33b}$$

Similar to Algorithm 1, an ARCD routine has been developed, but is not shown here due to space constraints. Below, the LPF

Algorithm 1: RTSC.

Input: n_{ps}, n_{prd}, $n_{\max}$, λ, γ, $\widehat{n}_{\mathrm{ip},0}$, $\widehat{a}_0$, and P_0;
Output: $\widehat{\theta}_k = [\widehat{a}_k, \widehat{n}_{\mathrm{ip},k}]^{\mathrm{T}}$;
$\Lambda = 2\pi/n_{\mathrm{prd}}$, $\widehat{\mu}_0 \leftarrow 0$;
while $k \geqslant 1$ **do**
  acquire $i^*_{2,k}$ and record the counter value $n_{\mathrm{cnt},k}$;
  compute the phase and prediction error

$$\psi_k = \mathrm{round}\left(n_{\mathrm{cnt},k} + \widehat{n}_{\mathrm{ip},k-1}\right)\Lambda$$
$$e_k = i^*_{2,k} - \widehat{a}_{k-1}\sin\left(\psi_k\right);$$

  compute the partial derivatives of $-e_k$ with respect to a and n_{ip} according to (16)

$$\phi_k^{\mathrm{T}} = \left[\sin\left(\psi_k\right) \quad \widehat{a}_{k-1}\cos\left(\psi_k\right)\Lambda\right];$$

  perturb the covariance matrix P_{k-1} and compute the gain vector L_k according to (24)

$$L_k = \frac{P_{k-1}\phi_{k|k-1}}{\lambda + \phi_k^{\mathrm{T}} P_{k-1}\phi_k};$$

  compute the parameter increment

$$\Delta\widehat{\theta}_k = L_k e_k;$$

  while $|\Delta\widehat{\theta}_k(2)| > n_{\max}$ **do**
    $\Delta\widehat{\theta}_k = \Delta\widehat{\theta}_k/2$;
  end
  update the parameters

$$\widehat{a}_k = \widehat{a}_{k-1} + \Delta\widehat{\theta}_k(1)$$
$$\widehat{\mu}_k = \widehat{\mu}_{k-1} + \gamma\Delta\widehat{\theta}_k(2)$$
$$\widehat{n}_{\mathrm{ip},k} = \widehat{n}_{\mathrm{ip},k-1} + \Delta\widehat{\theta}_k(2) + \widehat{\mu}_k;$$

  if $\widehat{a}_k < 0$ **then**
    $\widehat{a}_k = -\widehat{a}_k$, $\widehat{n}_{\mathrm{ip},k} = \widehat{n}_{\mathrm{ip},k} + n_{\mathrm{prd}}/2$;
  end
  while $\widehat{n}_{\mathrm{ip},k} \notin (0, n_{\mathrm{prd}}]$ **do**
    if $\widehat{n}_{\mathrm{ip},k} > n_{\mathrm{prd}}$ **then**
      $\widehat{n}_{\mathrm{ip},k} = \widehat{n}_{\mathrm{ip},k} - n_{\mathrm{prd}}$;
    else
      $\widehat{n}_{\mathrm{ip},k} = \widehat{n}_{\mathrm{ip},k} + n_{\mathrm{prd}}$;
    end
  end
  update the covariance matrix

$$P_k = \frac{1}{\lambda}\left(P_{k-1} - L_k\phi_k^{\mathrm{T}}P_{k-1}\right);$$

  compute counter-compare module register values according to (28) and (29);
  $\widehat{\theta}_k = [\widehat{a}_k, \widehat{n}_{\mathrm{ip},k}]^{\mathrm{T}}$, $k \leftarrow k+1$;
end

used in ARCD takes a Butterworth filter form

$$G(p) = \frac{\omega_{\mathrm{n}}^2}{p^2 + 1.414\omega_{\mathrm{n}}p + \omega_{\mathrm{n}}^2} \tag{34}$$

in which p is the differentiation operator and ω_{n} is the natural frequency.

TABLE II
MAIN PARAMETERS OF THE SS WPT SYSTEM

Symbol	Item	Value
C_{p}	Primary series compensation capacitor	49.9 nF
C_{s}	Secondary series compensation capacitor	49.5 nF
C_{f}	Output filter capacitor	504.4 μF
L_{p}	Self-inductance of the primary coil	200.9 μH
L_{s}	Self-inductance of the secondary coil	201.6 μH
M	Mutual inductance	39.7 μH
R_{o}	Load resistance	10 Ω
V_{d}	Input dc voltage	200 V

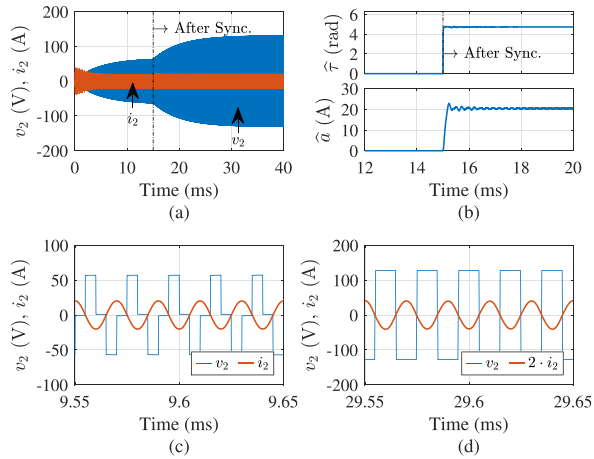

Fig. 6. Simulation results for the normal test using ARCD. (a) Envelopes of the rectifier input voltage v_2 and current i_2. (b) Estimated initial phase τ and amplitude a. (c) Zooming-in part of v_2 and i_2 before synchronization. (d) Zooming-in part of v_2 and i_2 after synchronization.

A. Comparison of Tracking Performance

Here, the proposed method is validated in Simscape of MATLAB. The convergence rates of a and τ are determined by the natural frequency ω_{n} in the ACRD method. For comparison purposes, two values for ω_{n} are tested, i.e., 2000 and 20 000 rad/s. The data-generating system is chosen as the SS system shown in Fig. 1(a), and the main parameters of this system is listed in Table II. Three tests under the following conditions are conducted to verify the performance of the ARCD method (assuming ZPA operation with $\delta = \pi$ rad).

1) Normal test: The primary and secondary PWM frequencies are the same, i.e., $f_1 = f_2 = 50$ kHz, the PS angle $\sigma = 0$ rad/s, and $\omega_{\mathrm{n}} = 20\,000$ rad/s. The initial phase τ is set to zero at beginning, and the active bridge is operated at the diode bridge mode when $t < 15$ ms by setting the driving signals of the switches to zero. The ACRD method starts to operate after $t = 15$ ms. The results are presented in Fig. 6, which shows that the ARCD finally achieves ZPA operation.
2) Envelope oscillation test: The conditions in this test are the same as in the first test, except for the PS angle which is changed as $\sigma = 0.4\,\pi$ rad. It has been found that envelope oscillation in i_2 is always encountered in synchronous switching, particularly when the estimated τ is not so smooth. For $\omega_{\mathrm{n}} = 20\,000$ rad/s which is relatively

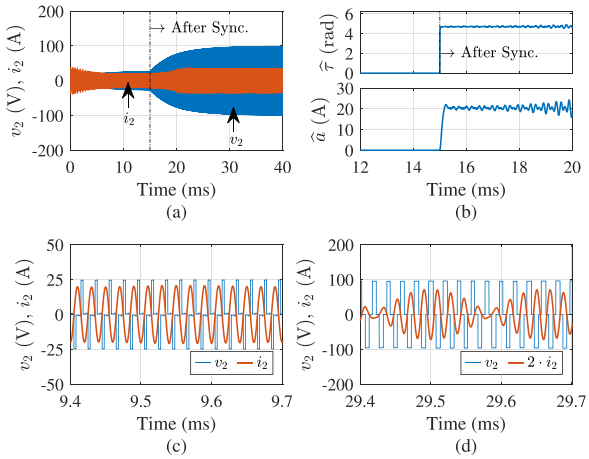

Fig. 7. Simulation results for the envelope oscillation test using ARCD. (a) Envelopes of v_2 and i_2. (b) Estimated τ and a. (c) Zooming-in part of v_2 and i_2 before synchronization. (d) Zooming-in part of v_2 and i_2 after synchronization.

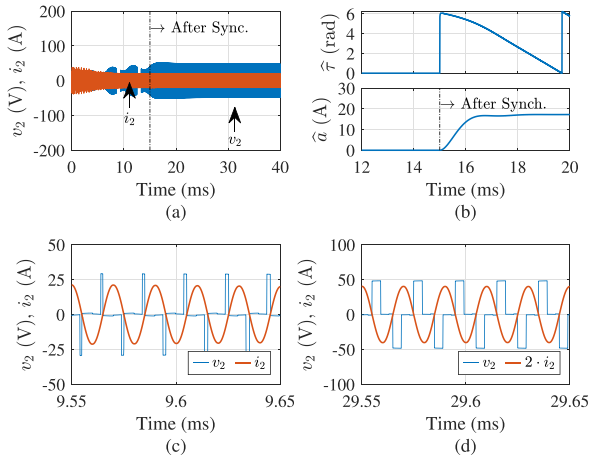

Fig. 8. Simulation results for the frequency mismatch test using ARCD. (a) Envelopes of v_2 and i_2. (b) Estimated τ and a. (c) Zooming-in part of v_2 and i_2 before synchronization. (d) Zooming-in part of v_2 and i_2 after synchronization.

large, the LPF provides poor attenuation of the high-order harmonics originating from the last terms of (31) on the right sides, so the estimated τ possibly suffers from harmonic distortions, leading to envelope oscillation. This is confirmed by Fig. 7(a) and (d), where a clear oscillation in the envelope of i_2 can be observed. It can be inferred that the most effective way to suppress envelope oscillation is to reduce $\omega_{\rm n}$.

3) Frequency mismatch test: In real applications, the clock periods of the primary and secondary DSPs are always not the same, due to factors such as the manufacture errors in crystal oscillators, or the use of variable frequency control on the primary side. When a mismatch between primary and secondary frequencies occurs, the power transferred to the load would fluctuate if no synchronous switching control is performed. The conditions in this test are the same as in the second test, except for the secondary frequency which is changed as $f_2 = 50.25$ kHz (0.5% deviation), and $\omega_{\rm n}$ which is changed as 2000 rad/s to suppress the envelope oscillation in i_2. The results are shown in Fig. 8. Interestingly, the estimated τ varies with respect to time because $f_1 \neq f_2$, which coincides with the analysis in Remark 2. However, as evidenced from Fig. 8(d), v_2 and i_2 are not ZPA, because the value of $\omega_{\rm n}$ is too small, and the delay introduced by the filter dynamics greatly slows down the tracking rate for τ.

Next, we proceed to evaluate the performance of the RTSC method. We only consider the third test which is the most challenging one among the three tests. The rectifier input current i_2 is sampled at the rate of 278 kS/s to obtain the data for RTSC. To improve the convergence of recursive parameter estimation, the forgetting factor is set as $\lambda = 0.999$, and initial parameter vector and covariance matrix are

$$\widehat{\theta}_0 = \begin{bmatrix} 0.01 \\ 0 \end{bmatrix}, \quad P_0 = \begin{bmatrix} 10^3 & 0 \\ 0 & 10^3 \end{bmatrix}. \tag{35}$$

The results are shown in Fig. 9. Clearly, the RTSC method successfully achieves the ZPA operation irrespective the pres-

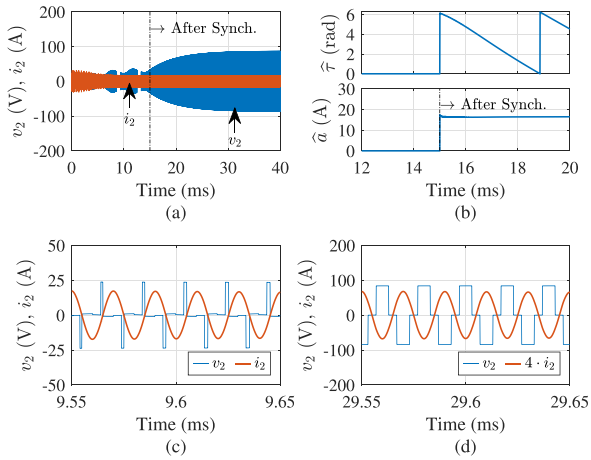

Fig. 9. Simulation results for the frequency mismatch test using RTSC. (a) Envelopes of v_2 and i_2. (b) Estimated τ and a. (c) Zooming-in part of v_2 and i_2 before synchronization. (d) Zooming-in part of v_2 and i_2 after synchronization.

mismatch. The simulation results demonstrate that the proposed RTSC method can perform as good as, or even better than the conventional ARCD method.

B. Comparison Under Harmonic Distortions

In a WPT system with high-order compensation, the input current of the active rectifier may contain a significant amount of high-order harmonic components, making the fundamental more challenging to track. In this section, we compare the robustness of the RTSC and ARCD methods in the presence of harmonic distortions. The LCC–LCC WPT system in Fig. 1(b) is considered and its parameters are illustrated in Table III. In this simulation, we assume ZPA operation, $\sigma = 0$ rad/s, $f_1 = 50$ kHz, and $f_2 = 50.25$ kHz. The initial parameters of RTSC are chosen as (35), the data sampling rate for i_2 is 278 kS/s, while the natural frequency of the LPF for ARCD is $\omega_{\rm n} = 2000$ rad/s. The simulation results are shown in Figs. 10 and 11. Note

TABLE III
MAIN PARAMETERS OF THE LCC–LCC WPT SYSTEM

Item	Symbol	Value
Primary series compensation capacitor	C_{p}	63.1 nF
Primary parallel compensation capacitor	C_{pr}	243.8 nF
Secondary series compensation capacitor	C_{s}	62.4 nF
Secondary parallel compensation capacitor	C_{sr}	245.5 nF
Output filter capacitor	C_{f}	504.4 μF
Self-inductance of the primary coil	L_{p}	202.5 μH
Primary parallel compensation inductor	L_{pr}	41.8 μH
Self-inductance of the secondary coil	L_{s}	207.9 μH
Secondary parallel compensation inductor	L_{sr}	41.3 μH
Mutual inductance	M	58.0 μH
Load resistance	R_{o}	30 Ω
Input dc voltage	V_{d}	200 V

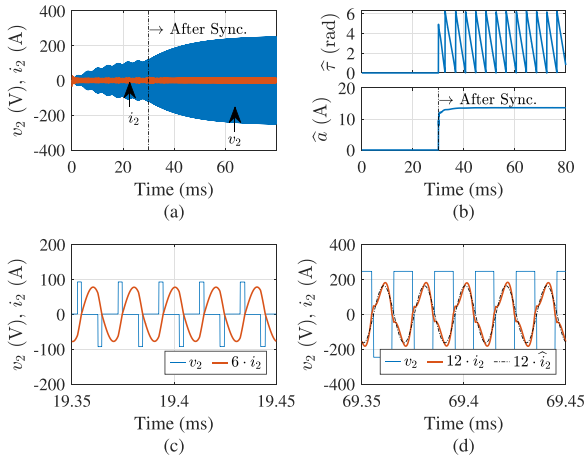

Fig. 10. Simulation results for the harmonic distortion test under frequency mismatch using RTSC. (a) Envelopes v_2 and i_2. (b) Estimated τ and a. (c) Zooming-in part of v_2 and i_2 before synchronization. (d) Zooming-in part of v_2, i_2, and $\widehat{i_2}$ after synchronization.

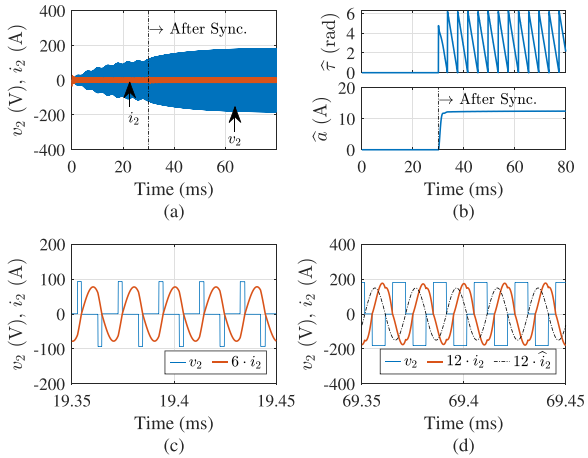

Fig. 11. Simulation results for the harmonic distortion test under frequency mismatch using ARCD. (a) Envelopes of v_2 and i_2. (b) Estimated τ and a. (c) Zooming-in part of v_2 and i_2 before synchronization. (d) Zooming-in part of v_2, i_2, and $\widehat{i_2}$ after synchronization.

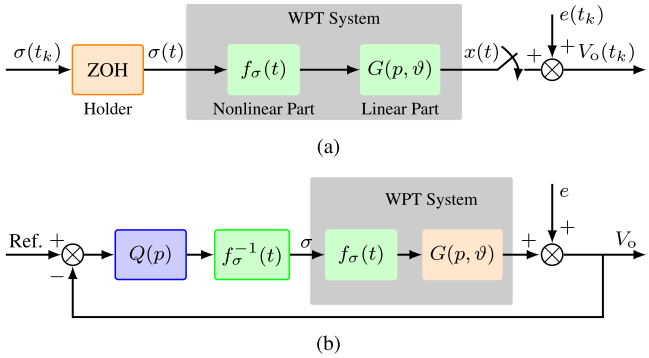

Fig. 12. Control structure. (a) Block diagram of the Hammerstein model. (b) Control diagram of based on the Hammerstein model.

panels of Figs. 10 and 11 have been scaled to better show the distortions in i_2. The simulations results illustrate that even if the current distortion is quite significant, the RTSC method provides satisfactory synchronization performance and outperforms the ARCD method, as evidenced from Figs. 10(d) and 11(d) that the prediction $\widehat{i_2}$ generated from the estimated $\widehat{a}$ and $\widehat{\tau}$ fits better the measurement data in the RTSC case.

IV. CONTROL DESIGN

In this section, a PID controller will be designed to regulate the load power on the secondary side for the SS WPT system. A mathematical model that relates the PS angle of the active rectifier and the load voltage will be established, and then used as for control parameter tuning.

A. Model Identification

According to (11), i_2 is constant and decoupled with the load, so the power flowing through the rectifier can be controlled by σ. As shown in (7b), the rectified current I_{r} has a static nonlinear dependence on $|I_2|$, i.e., $f_\sigma = \cos(\sigma/2)$ in the ZPA state, while C_{f} and R_{o} after the rectifier form a linear network, so it is reasonable to use the following Hammerstein model to describe the relationship between σ and V_{o} [see also Fig. 12(a)]:

$$\begin{cases} x(t) = G(p,\vartheta) f_\sigma(t) = \frac{B(p,\vartheta)}{A(p,\vartheta)} f_\sigma(t) \\ V_{\mathrm{o}}(t_k) = x(t_k) + e(t_k) \end{cases} \tag{36}$$

in which $e(t_k)$ is measurement noise, $t_k = kT$ is sampling instant, T is the sampling period, and p is the differential operator.

$A(p,\vartheta)$ and $B(p,\vartheta)$ are the following polynomials:

$$A(p,\vartheta) = p^{n_\alpha} + \alpha_1 p^{n_\alpha - 1} + \cdots + \alpha_{n_\alpha} \tag{37a}$$

$$B(p,\vartheta) = \beta_0 p^{n_\beta} + \beta_1 p^{n_\beta - 1} + \cdots + \beta_{n_\beta} \tag{37b}$$

where $\vartheta = [\alpha_1, \cdots \alpha_{n_\alpha}, \beta_0, \ldots, \beta_{n_\beta}]^{\mathrm{T}}$ is the vector of unknown parameters, with n_α and n_β ($n_\alpha \geq n_\beta$) being polynomial degrees. ϑ can be estimated from sampled input–output data

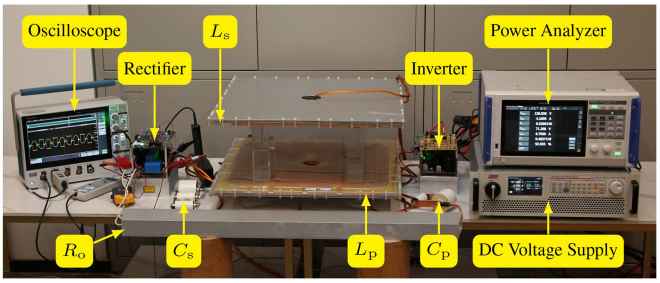

Fig. 13. Laboratory prototype.

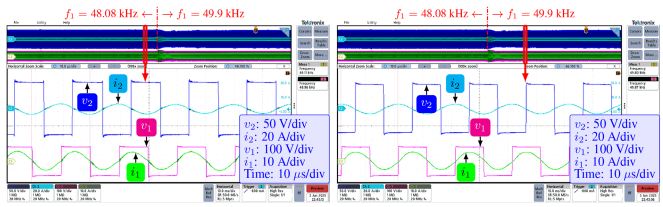

(a) (b)

Fig. 14. Oscilloscope screen shots for the detuning to resonance test. (a) Waveform in the detuning state. (b) Waveform in the resonance state.

$\{\sigma(t_k), V_o(t_k)\}_{k=1}^N$, by minimizing the following cost function:

$$\hat{\vartheta} = \arg\min_{\vartheta} \frac{1}{2N} \sum_{k=1}^{N} [V_o(t_k) - x(t_k)]^2 . \tag{38}$$

The above-mentioned parameter estimation problem can be solved by using the refined instrumental variable method. To save space, this method will not be reproduced here, and the reader is directed to [46] and the references therein for more details. Note that the Hammerstein model (36) could not be so accurate if the load varies in a wide range. When the load is time varying, the linear parameter varying Hammerstein model presented in [47] could be a better choice. Another option is to track online the Hammerstein model parameters using a recursive algorithm presented in [46], but this approach is only effective when the load is slowly varying.

B. Control Parameter Tuning

The model structure analysis implies that if the input nonlinearity $f_\sigma(t)$ has been compensated for, the rest of the system consisting of C_f and R_o is a linear network and, therefore, linear control such as PID can be applied to regulate the load voltage. The control diagram is illustrated in Fig. 12(b), where $Q(p)$ is the PID controller. Denoting by K_p the proportional gain, K_i the integral gain, and K_d the differential gain, $Q(p)$ is expressed as

$$Q(p) = K_p + K_i \frac{1}{p} + K_d p \tag{39}$$

where the three parameters K_p, K_i, and K_d can be tuned either by experience or based on the linear transfer function of (36). The latter option is adopted because it is easier to implement and several mature tool are available, such as the pidtune routine in the control system toolbox of MATLAB.

V. Validation of Active Rectification

The proposed method is validated on a prototype with SS topology shown in Fig. 13 and a prototype with LCC–LCC topology (photo not shown here). The algorithm is implemented on DSP TMS320F28377D, and data are sampled by AD9226. The SiC MOSFETs C3M0021120 K from Wolfspeed are selected as the switches. The main parameters of the circuit components and coupler under 20 cm coil distance are listed in Table II for the SS topology and Table III for the LCC–LCC topology, except for the dc voltage supply which is changed as 100 V.

There are five experiments having been conducted, and the results are presented in the following subsections. Except for the experiment in Section V-D, the rectifier input current is sampled at 278 kS/s, which corresponds to a 3.6 μs sampling interval, the forgetting factor is set as $\lambda = 0.99$, and the integration parameter is set as $\gamma = 0.01$. $\widehat{\theta}_0$ and P_0 are selected as

$$\widehat{\theta}_0 = \begin{bmatrix} 1 \\ 0 \end{bmatrix}, \quad P_0 = \begin{bmatrix} 10^3 & 0 \\ 0 & 10^3 \end{bmatrix}. \tag{40}$$

In all experiments, the ZVS operation is configured, and the counter-compare registers of the PWM module parameters are only refreshed once per each PWM period when the counter reaches zero.

A. Detuning to Resonance Test

In this experiment, the tracking performance of the RTSC method is verified based on the SS WPT system considering a detuning to resonance state transition. More exactly, the primary PWM frequency is initially set as $f_1 = 48.08$ kHz, and then changed to 49.9 kHz at some instant, while the secondary PWM frequency is fixed as $f_2 = 50$ kHz. The PS angle is $\sigma = 0$ during the whole process.

The oscilloscope screen shots of this process are shown in Fig. 14, and the parameter estimation results are shown in Fig. 15. Clearly, the amplitude of i_2 after the change of f_1 restores to its steady-state value in about 1.3 ms, as shown in Fig. 15(b), which indicates that the proposed method maintains good synchronization capability even when the resonant state of the system changes.

B. Coil Spacing Test

In real applications, coupling distance variation is commonly encountered. To emulate this, the tracking performance of the proposed method is verified when the coupling distance of the SS WPT system deviates from the nominal 20 to 10 cm. When the distance between the primary and secondary coils is adjusted from 20 to 10 cm, we have $L_p = 214.8$ μH, $L_s = 216.8$ μH, and $M = 98.5$ μH. Fig. 16 presents the voltage and current waveforms before and after synchronization when the coil distance changes along the vertical direction, and Fig. 17 shows that the proposed method performs very well in this situation.

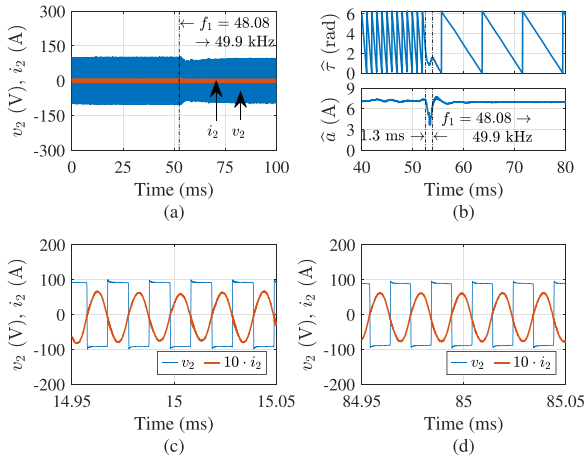

Fig. 15. Experimental results for the detuning to resonance test ($f_1 = 48.08 \rightarrow 49.9$ kHz, $f_2 = 50$ kHz). (a) Envelopes of v_2 and i_2. (b) Estimated τ and a. (c) Zooming-in part of v_2 and i_2 in detuning state. (d) Zooming-in part of v_2 and i_2 in resonance state.

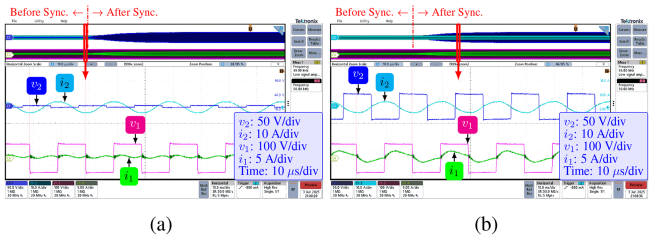

Fig. 16. Oscilloscope screen shots after the coil spacing changes from 20 to 10 cm. (a) Waveform before synchronization. (b) Waveform after synchronization.

C. Abrupt PS Angle Variation Test

The PS control is a widely used technique to regulate the load power of the system. Here, let us consider the LCC–LCC WPT system. As shown in Figs. 18 and 19, the good synchronization performance in the dynamic process of increasing and decreasing PS angles can be observed. These results indicate that the proposed method can maintain good synchronization ability even with changes in the PS angle.

D. Sampling Frequency Test

To further evaluate the effect of sampling rate on the proposed synchronization method, we reduce the sampling rate of the secondary current i_2 of the LCC–LCC WPT system to $f_s = 167$ and 125 kS/s. With the system load fixed at 20 Ω, the forgetting factor values are configured as 0.9835 ($f_s = 167$ kS/s) and 0.9781 ($f_s = 125$ kS/s). The synchronization performance under these different sampling conditions is presented in Fig. 20, while the parameter estimation results are presented in Figs. 21 and 22, which corresponds to the sampling rate of 167 and 125 kS/s, respectively. It can be observed that the proposed method achieves satisfactory synchronization performance for both sampling rates.

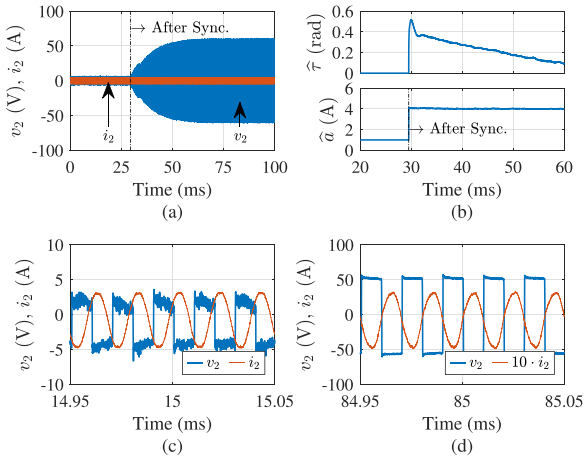

Fig. 17. Experimental results for the coil spacing variation test when the coil distance is 10 cm. (a) Envelopes of v_2 and i_2. (b) Estimated τ and a. (c) Zooming-in part of v_2 and i_2 before synchronization. (d) Zooming-in part of v_2 and i_2 after synchronization.

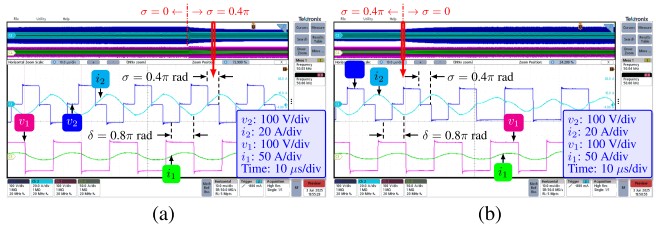

Fig. 18. Oscilloscope screen shots for the PS angle variation test. (a) $\sigma = 0 \rightarrow 0.4\pi$ rad. (b) $\sigma = 0.4\pi \rightarrow 0$ rad.

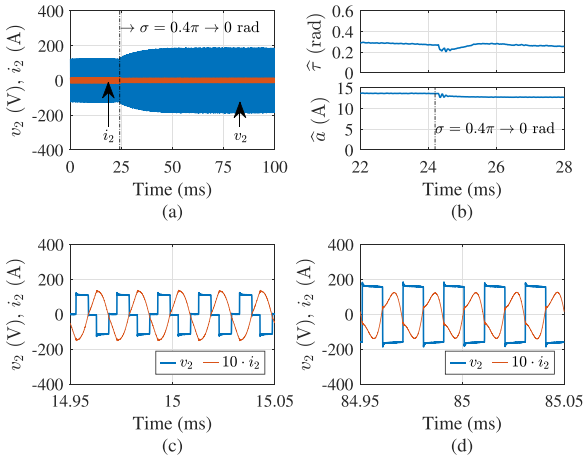

Fig. 19. Experimental results for the PS angle variation test ($\sigma = 0 \rightarrow 0.4\pi$ rad). (a) Envelopes of v_2 and i_2. (b) Estimated τ and a. (c) Zooming-in part of v_2 and i_2 before the change of PS angle. (d) Zooming-in part of v_2 and i_2 after the change of PS angle.

For both sampling rates, the convergence times are both lower than 1 ms. While higher sampling frequencies allow for faster parameter updates, it inevitably increases the computational load. Therefore, we need to balance between sampling rate selection and software processing time.

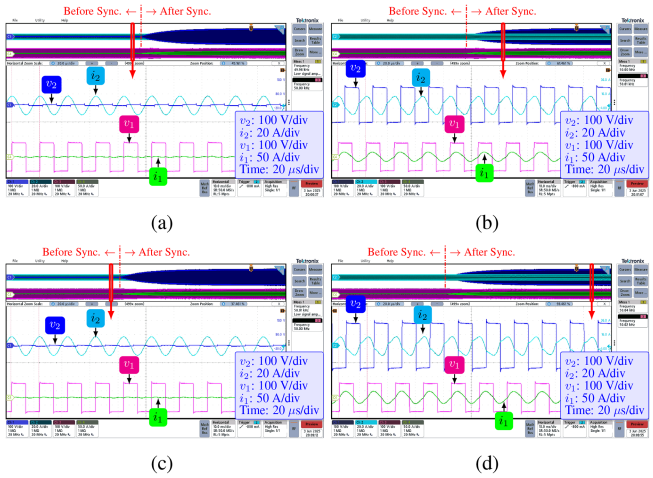

Fig. 20. Oscilloscope screen shots for the sampling rate test. (a) Waveform before synchronization with $f_s = 167$ kS/s. (b) Waveform after synchronization with $f_s = 167$ kS/s. (c) Waveform before synchronization with $f_s = 125$ kS/s. (d) Waveform after synchronization with $f_s = 125$ kS/s.

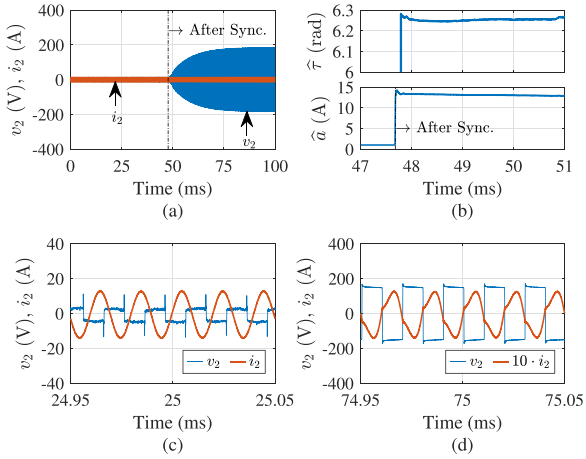

Fig. 21. Experimental results for the sampling rate test with $f_s = 167$ kS/s. (a) Envelopes of v_2 and i_2. (b) Estimated τ and a. (c) Zooming-in part of v_2 and i_2 before synchronization. (d) Zooming-in part of v_2 and i_2 after synchronization.

E. Harmonic Distortion Test

For the LCC–LCC WPT system, the distortion of i_2 is dependent on the load resistance. Here, we test the load resistance of 20 and 30 Ω to obtain different harmonic distortions in i_2. The corresponding waveforms are shown in Fig. 23, and the experimental results are presented in Figs. 24 and 25, which demonstrate that the proposed method is insensitive to harmonic distortions.

The power and efficiency measured by HIOKI PW8001 are shown in Fig. 26, where U_{dc1}, I_{dc1}, and P_{dc1} represent, respectively, the voltage, current, and power of the dc power supply, while U_{dc2}, I_{dc2}, and P_{dc2} represent, respectively, the voltage, current, and power of the load.

As regards the computational burden in implementation using TMS320F28377D, each recursion of RTSC consumes about 416

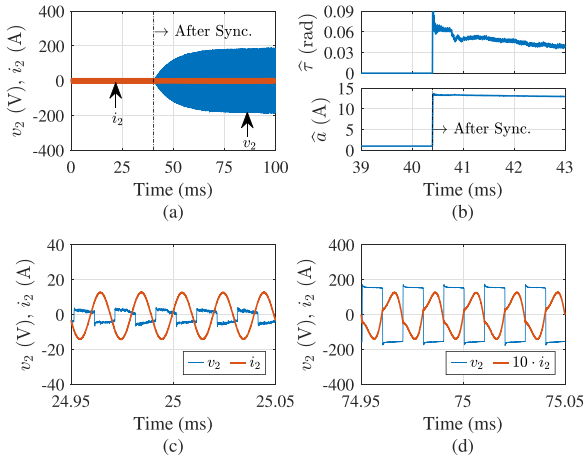

Fig. 22. Experimental results for the sampling rate test with $f_s = 125$ kS/s. (a) Envelopes of v_2 and i_2. (b) Estimated τ and a. (c) Zooming-in part of v_2 and i_2 before synchronization. (d) Zooming-in part of v_2 and i_2 after synchronization.

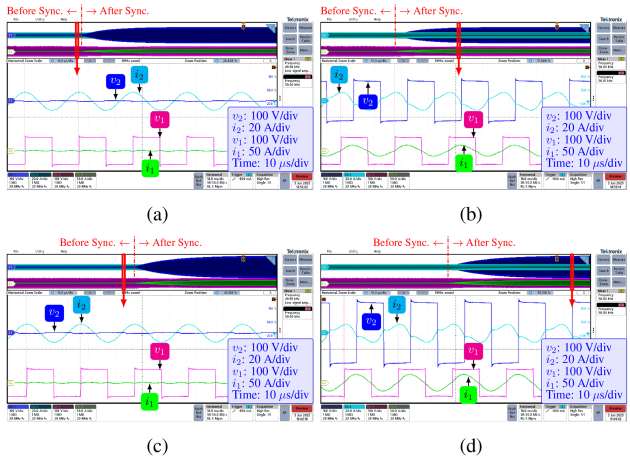

Fig. 23. Oscilloscope screen shots for the harmonic distortion test. (a) Before synchronization with $R_o = 20\ \Omega$. (b) After synchronization with $R_o = 20\ \Omega$. (c) Before synchronization for $R_o = 30\ \Omega$. (d) After synchronization for $R_o = 30\ \Omega$.

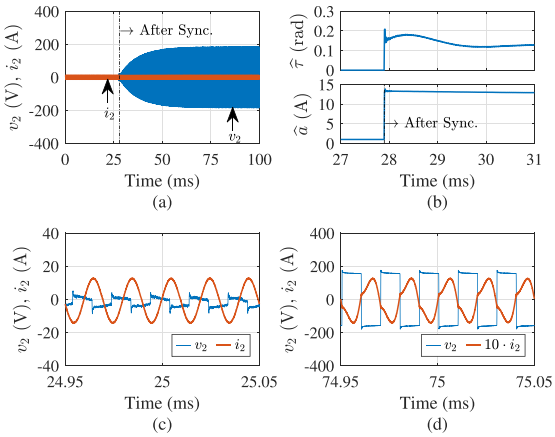

Fig. 24. Experimental results for the harmonic distortion test with $R_o = 20\ \Omega$. (a) Envelopes of v_2 and i_2. (b) Estimated τ and a. (c) Zooming-in part of v_2 and i_2 before synchronization. (d) Zooming-in part of v_2 and i_2 after synchronization.

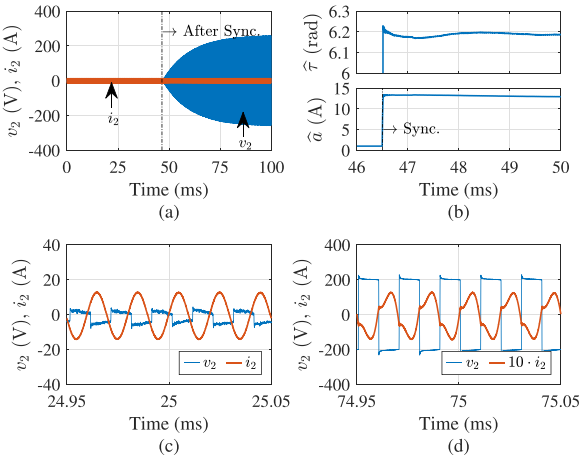

Fig. 25. Experimental results for the harmonic distortion test with $R_o = 30\,\Omega$. (a) Envelopes of v_2 and i_2. (b) Estimated τ and a. (c) Zooming-in part of v_2 and i_2 before synchronization. (d) Zooming-in part of v_2 and i_2 after synchronization.

Fig. 26. Power and efficiency of the LCC–LCC WPT system for the harmonic distortion test. (a) $R_o = 20\,\Omega$. (b) $R_o = 30\,\Omega$.

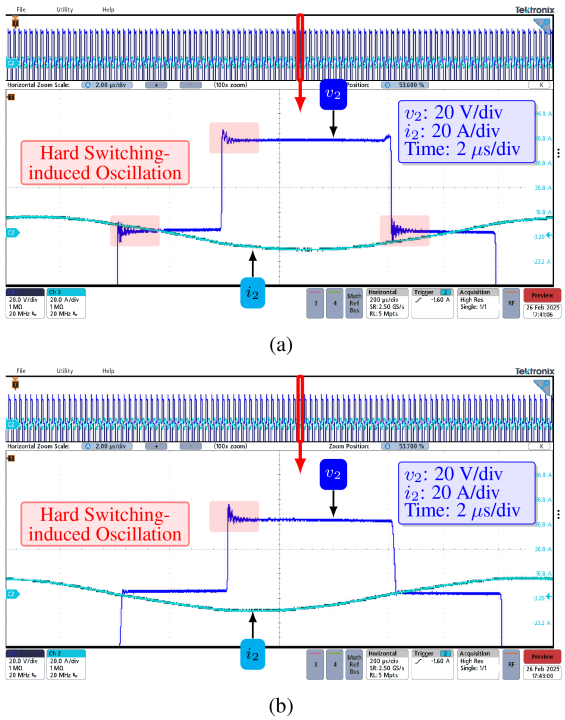

Fig. 27. Oscillation during switching. (a) ZPA operation. (b) ZVS operation.

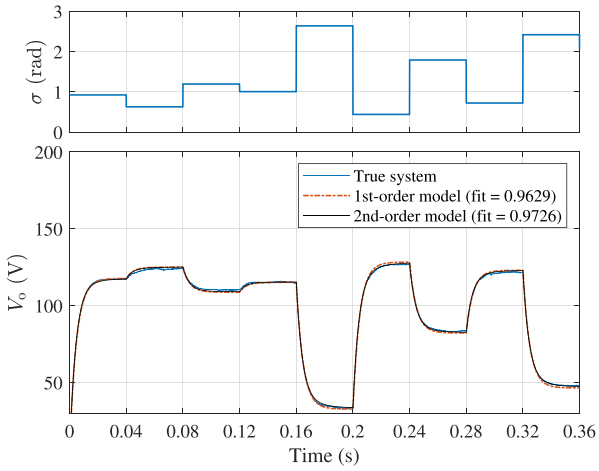

Fig. 28. Input and output data for model identification.

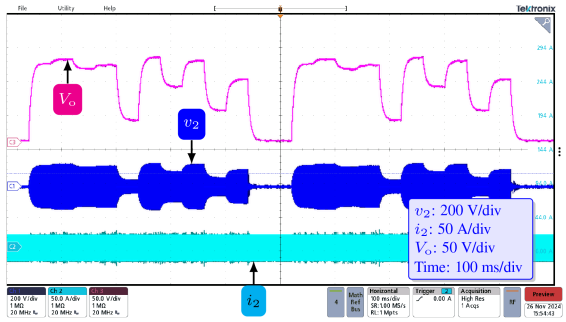

Fig. 29. Oscilloscope screenshot of the data for model identification.

clocks (2.0 μs), and the details are as follows: the data acquisition from AD9226 consumes 97 clocks, the recursive parameter estimation (24) consumes 194 clocks, the computation of counter-compare register values for the enhanced PWM module consumes 99 clocks, and the update of the counter-compare registers consumes 26 clocks. The sampling period of i_2 is 3.6 μs, which is enough to complete all the computation.

Finally, Fig. 27 shows two zooming-in parts of the voltage oscillation during switching. When the system is in the ZPA state, high-frequency oscillation caused by hard switching occurs at both the rising and falling edges of the voltage. However, in the ZVS state, the voltage oscillation only occurs at the positive rising edge. Fortunately, the oscillations are not so obvious because SiC MOSFETs are used.

VI. Validation of Load Voltage Control

A. Model Identification

To generate informative data for model identification, a random PS angle is chosen to excite the SS WPT system. The input–output data for model identification are shown in Fig. 28, where the load voltage is subsampled from the oscilloscope data shown in Fig. 29 at the rate of 10 kS/s. In the oscilloscope screenshot, Ch1 and Ch2 represent, respectively, the input

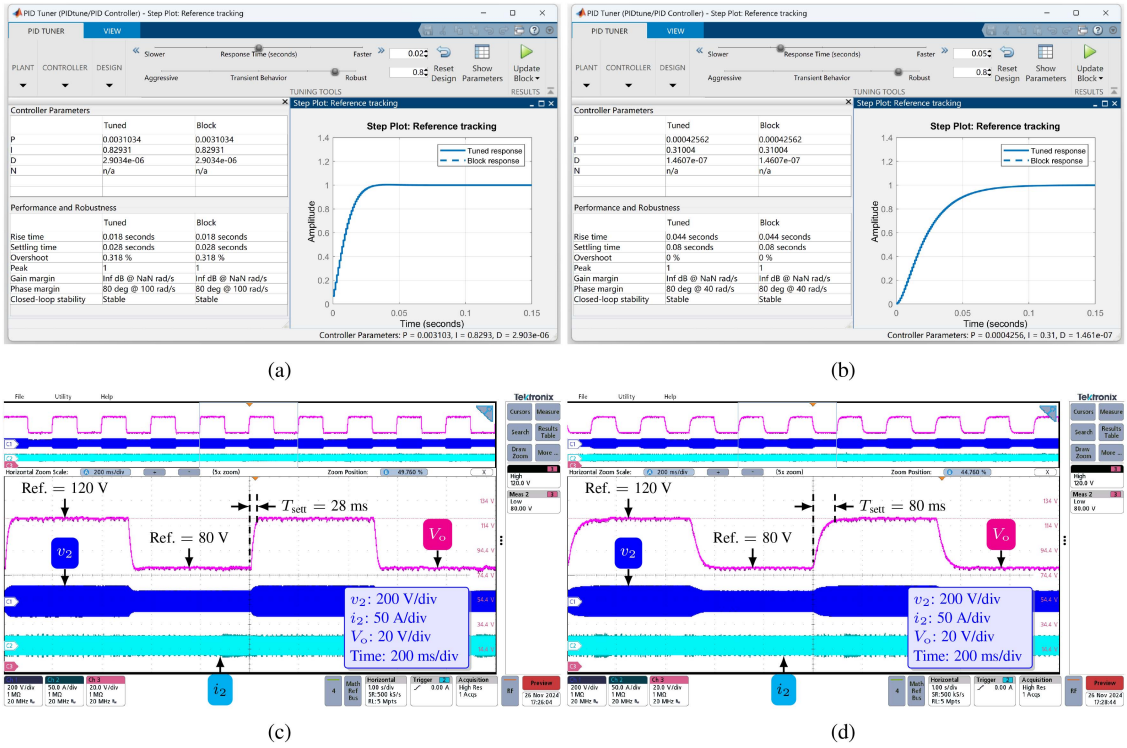

Fig. 30. PID control results. (a) Fast PID controller tuning. (b) Slow PID controller tuning. (c) Controlled load voltage with the fast controller. (d) Controlled load voltage with the slow controller.

TABLE IV
ESTIMATED MODEL PARAMETERS

Order	$\widehat{\alpha}_1$	$\widehat{\alpha}_2$	$\widehat{\beta}_0$	$\widehat{\beta}_1$	fit
1	209.4	—	$2.751 \cdot 10^4$	—	0.9629
2	277	$1.09 \cdot 10^4$	$2.862 \cdot 10^4$	$1.435 \cdot 10^6$	0.9726

voltage v_2 and current i_2 of the active rectifier, and Ch3 represents the load voltage V_o. Based on the sampled input–output data, the parameters of the following first- and second-order models

$$G(p,\vartheta) = \frac{\beta_0}{p+\alpha_1}, \quad G(p,\vartheta) = \frac{\beta_0 p + \beta_1}{p^2 + \alpha_1 p + \alpha_2} \tag{41}$$

are estimated by the tfrivc routine in [46] and listed in Table IV.

The accuracy of the model is evaluated by the fitness ratio, which is defined in the following:

$$\text{fit} = 1 - \frac{\|V_o^* - \widehat{V}_o\|}{\|V_o^* - \text{mean}\{V_o^*\}\|} \tag{42}$$

where V_o^* is the measured version of V_o, and $\widehat{V}_o$ is the prediction of V_o using an identified model. As can be seen from Table IV, both models are very accurate (fit $\geqslant 0.96$), indicating that a first-order model is fairly enough to describe the dominant dynamic behavior of the system. Furthermore, a comparison between the measured output and the estimated model output is shown in the bottom panel of Fig. 28.

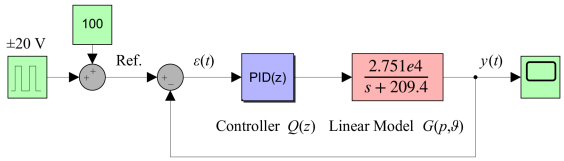

Fig. 31. Simulink model used for PID tuning.

B. PID Control

Based on the identified first-order model

$$G(p,\vartheta) = \frac{2.751 \cdot 10^4}{p + 209.4} \tag{43}$$

discrete-time PID controllers of the form

$$Q(z) = K_\text{p} + K_\text{i}\frac{T_\text{c}}{z-1} + K_\text{d}\frac{z-1}{zT_\text{c}} \tag{44}$$

where $T_\text{c} = 1$ ms is the control period, are designed to regulate the load voltage. The control parameters are tuned using the pidtune routine from the MATLAB control system toolbox, which requires to provide two performance indexes, i.e., response time and transient behavior shown in the top panels of Fig. 30, and the closed-loop Simulink model shown in Fig. 31. Two PID controllers are designed (see Table V for the tuned parameters), the first one pursuing tracking performance and the second one pursuing robustness. The transient behavior parameter for both controllers is fixed as 0.8, while the response time parameter is set as 0.02 for the fast controller and 0.05 for

TABLE V
PID CONTROLLER PARAMETERS

No.	K_{p}	K_{i}	K_{d}
1	$3.1034 \cdot 10^{-3}$	$8.2931 \cdot 10^{-1}$	$2.9034 \cdot 10^{-6}$
2	$4.2562 \cdot 10^{-4}$	$3.1004 \cdot 10^{-1}$	$1.4607 \cdot 10^{-7}$

the slow controller, which corresponds to settling time of 28 and 80 ms.

The reference inputs of the closed-loop systems are chosen as a square wave alternating between 120 and 80 V, with a switching period of 1.0 s. Fig. 30(c) and 30(d) show the controlled load voltage of the two closed-loop systems. Clearly, the settling time (T_{sett}) of the rising edge is approximately 28 ms for the fast controller, while this value increases to about 80 ms for the slow controller, with no overshoot. These results confirm that the reference tracking performance is in agreement with the design objective.

VII. CONCLUSION

This article has proposed a secondary-side control method for SS and LCC–LCC WPT systems with an active rectifier. The proposed method consists of three steps. First, a recursive algorithm was used to track in real time the amplitude and phase of the rectifier input current from sampled data and, on this basis, the switches of the active rectifier were controlled to adjust amplitude and angle of the equivalent load impedance. Afterward, a Hammerstein model was identified to characterize the relationship between the PS and the load voltage. Finally, PID controllers were designed based on the identified model to regulate the load voltage. A 1.5-kW level prototype was built to verify the effectiveness of the proposed control method. The proposed method is computationally efficient: when using TMS320F28377D as the controller, the recursive tracking algorithm can run at 278 kS/s without any problem.

REFERENCES

[1] S. Roy, A. N. M. W. Azad, S. Baidya, M. K. Alam, and F. Khan, "Powering solutions for biomedical sensors and implants inside the human body: A comprehensive review on energy harvesting units, energy storage, and wireless power transfer techniques," *IEEE Trans. Power Electron.*, vol. 37, no. 10, pp. 12237–12263, Oct. 2022.

[2] Z. Liu, Y.-G. Su, Y.-M. Zhao, A. P. Hu, and X. Dai, "Capacitive power transfer system with double T-type resonant network for mobile devices charging/supply," *IEEE Trans. Power Electron.*, vol. 37, no. 2, pp. 2394–2403, Feb. 2022.

[3] Y. Chen et al., "A clamp circuit-based inductive power transfer system with reconfigurable rectifier tolerating extensive coupling variations," *IEEE Trans. Power Electron.*, vol. 39, no. 2, pp. 1942–1946, Feb. 2024.

[4] J. Wu, Y. Li, X. Dai, R. Gao, and M. He, "A dynamic power transfer route construction and optimization method considering random node distribution for wireless power transfer network," *IEEE Trans. Power Electron.*, vol. 39, no. 4, pp. 4858–4869, Apr. 2024.

[5] X. Zhang et al., "A novel hybrid shielding method with single-source active topology and efficiency stability for wireless power transfer," *IEEE Trans. Magn.*, vol. 59, no. 11, pp. 1–6, Nov. 2023.

[6] C. Liang et al., "An anti-offset CPT system with multiple pickups for mobile desktop application," *IEEE Trans. Power Electron.*, vol. 39, no. 3, pp. 3826–3841, Mar. 2024.

[7] X. Liu, F. Gao, H. Niu, G. Sun, T. Wang, and H. Wang, "A series–parallel transformer-based WPT system for 400-V and 800-V electric vehicles with Z1 or Z2 class," *IEEE Trans. Power Electron.*, vol. 39, no. 1, pp. 1749–1761, Jan. 2024.

[8] Z. Deng et al., "Design of a 60-kW EV dynamic wireless power transfer system with dual transmitters and dual receivers," *IEEE J. Emerg. Sel. Topics Power Electron.*, vol. 12, no. 1, pp. 316–327, Feb. 2024.

[9] Z. Yan et al., "Free-rotation wireless power transfer system based on composite anti-misalignment method for AUVs," *IEEE Trans. Power Electron.*, vol. 38, no. 4, pp. 4262–4266, Apr. 2023.

[10] X. Zhang, G. Li, T. Chen, F. Wang, Q. Yang, and W. Xu, "A high-efficiency underwater hybrid wireless power transfer system with low plate voltage stresses," *IEEE Trans. Power Electron.*, vol. 39, no. 8, pp. 10546–10557, Aug. 2024.

[11] P. Bellitti et al., "A wearable and wirelessly powered system for multiple finger tracking," *IEEE Trans. Instrum. Meas.*, vol. 69, no. 5, pp. 2542–2551, May. 2020.

[12] Z. Xue, K. T. Chau, W. Liu, and Z. Hua, "Magnetic-free wireless self-direct drive motor system for biomedical applications with high-robustness," *IEEE Trans. Power Electron.*, vol. 39, no. 2, pp. 2882–2891, Feb. 2024.

[13] J. Wu, Z. Jin, X. Han, W. Zhang, Q. Zhao, and Z. Liang, "Construction and optimization of power transfer route in array wireless power transfer network with multiple load nodes," *IEEE Trans. Power Electron.*, vol. 39, no. 3, pp. 3842–3850, Mar. 2024.

[14] K. Chen et al., "A noncommunication mutual inductance estimation method for multiple transmitters SS-compensated dynamic wireless power transfer with low calculation effort," *IEEE Trans. Power Electron.*, vol. 39, no. 7, pp. 7803–7807, Jul. 2024.

[15] E. Abramov and M. M. Peretz, "Adaptive self-tuned controller IC for resonant-based wireless power transfer transmitters," *IEEE Trans. Power Electron.*, vol. 36, no. 11, pp. 12413–12431, Nov. 2021.

[16] S. Li et al., "Identification and H∞ robust control of wireless power transfer system by Hammerstein model," *IEEE Trans. Power Electron.*, vol. 39, no. 7, pp. 8883–8893, Jul. 2024.

[17] L. Wang, P. Sun, Y. Liang, L. He, X. Wu, and Q. Deng, "Research on the control strategy of communication-free IPT system based on multiparameter joint real-time identification," *IEEE Trans. Power Electron.*, vol. 39, no. 1, pp. 1912–1926, Jan. 2024.

[18] S. Zhao, C. Tang, F. Chen, D. Zhao, P. Deng, and J. Xiao, "Modeling and control of the WPT system subject to input nonlinearity and communication delay," *IEEE Trans. Power Electron.*, vol. 38, no. 11, pp. 14776–14787, Nov. 2023.

[19] M. Sun, X. Dai, Y. Su, Y. Li, and S. Zhao, "Frequency and phase synchronous control method without communication of the BCPT system," *IEEE Trans. Power Electron.*, vol. 39, no. 4, pp. 4792–4804, Apr. 2024.

[20] B. Zou and Z. Huang, "Primary-frequency-tuning and secondary-impedance-matching IPT converter with programmable constant power output and optimal efficiency tracking against variation of coupling coefficient," *IEEE Trans. Power Electron.*, vol. 39, no. 4, pp. 4895–4909, Apr. 2024.

[21] N. Pucci, C. Papavassiliou, and P. D. Mitcheson, "Synchronous operation of high-frequency inductive power transfer systems through injection locking," *IEEE Trans. Power Electron.*, vol. 38, no. 10, pp. 11984–11994, Oct. 2023.

[22] K. Colak, E. Asa, M. Bojarski, D. Czarkowski, and O. C. Onar, "A novel phase-shift control of semibridgeless active rectifier for wireless power transfer," *IEEE Trans. Power Electron.*, vol. 30, no. 11, pp. 6288–6297, Nov. 2015.

[23] R. Mai, Y. Liu, Y. Li, P. Yue, G. Cao, and Z. He, "An active-rectifier-based maximum efficiency tracking method using an additional measurement coil for wireless power transfer," *IEEE Trans. Power Electron.*, vol. 33, no. 1, pp. 716–728, Jan. 2018.

[24] P. Lawton, F. Lin, G. A. Covic, and D. J. Thrimawithana, "A wireless synchronization controller for high-power stationary and semi-dynamic wireless charging of electric vehicles," *IEEE Trans. Power. Electron.*, vol. 38, no. 11, pp. 13341–13352, Nov. 2023.

[25] Y. Zhang, S. Chen, X. Li, and Y. Tang, "Dual-side phase-shift control of wireless power performance is implemented on primary side based on driving windings," *IEEE Trans. Ind. Electron.*, vol. 68, no. 9, pp. 8999–9002, Sep. 2021.

[26] Y. Zhang, X. Li, S. Chen, and Y. Tang, "Soft switching for strongly coupled wireless power transfer system with 90 dual-side phase shift," *IEEE Trans. Ind. Electron.*, vol. 69, no. 1, pp. 282–292, Jan. 2022.

[27] C. Da, F. Li, L. Wang, C. Tao, S. Li, and M. Nie, "Pulse synchronization scheme for undersea BWPT system based on simultaneous wireless power and data transfer technology," in *IEEE Trans. Circuits Syst. II, Exp. Briefs*, vol. 72, no. 1, pp. 333–337, Jan. 2025.
[28] D. J. Thrimawithana, U. K. Madawala, and M. Neath, "A synchronization technique for bidirectional IPT systems," *IEEE Trans. Ind. Electron.*, vol. 60, no. 1, pp. 301–309, Jan. 2013.
[29] D. Zhang, M. Chen, B. Li, X. Wang, X. Sun, and F. Jiang, "Synchronization strategy based on resonant current detection for bidirectional wireless charging system," *IEEE Trans. Power Electron.*, vol. 37, no. 9, pp. 11436–11449, Sep. 2022.
[30] R. K. Yakala, D. P. Nayak, and S. K. Pramanick, "Input reactive power control of bidirectional WPT to improve system efficiency," *IEEE Trans. Ind. Appl.*, vol. 60, no. 4, pp. 5813–5824, Jul.–Aug. 2024.
[31] D. J. Thrimawithana, U. K. Madawala, and M. Neath, "A P&Q based synchronization technique for bi-directional IPT pick-ups," in *Proc. IEEE 9th Int. Conf. Power Electron. Drive Syst.*, 2011, pp. 40–45.
[32] Y. Tang, Y. Chen, U. K. Madawala, D. J. Thrimawithana, and H. Ma, "A new controller for bidirectional wireless power transfer systems," *IEEE Trans. Power Electron.*, vol. 33, no. 10, pp. 9076–9087, Oct. 2018.
[33] S. Zhao, Y. Li, D. Wu, and R. Mai, "Current-decomposition-based digital phase synchronization method for BWPT system," *IEEE Trans. Power Electron.*, vol. 36, no. 11, pp. 12183–12188, Nov. 2021.
[34] S. Jia, S. Duan, and C. Chen, "An I/Q phase detection-based harmonic-insensitive phase synchronization method for bidirectional wireless power transfer system," *IEEE Trans. Ind. Electron.*, vol. 71, no. 7, pp. 6955–6965, Jul. 2024.
[35] I. Hussain et al., "A phase-synchronization control of bidirectional wireless power transfer system for G2V and V2G operation modes," in *IEEE Trans. Transport. Electrific.*, 2025.
[36] S. Jia, S. Duan, C. Chen, and L. Gan, "Modeling, analysis, and design of phase synchronization loop for BIPT system considering operating point parameters variation," in *IEEE Trans. Circuits Syst. I., Reg. Papers*, vol. 72, no. 4, pp. 1962–1974, Apr. 2025.
[37] X. Wang, C. Q. Jiang, J. Zhou, W. Guo, Y. Fan, and L. Mo, "Synchronization method for wireless power transfer system by detecting voltage transient on a sensor inductor," in *IEEE Trans. Ind. Electron.*, vol. 72, no. 6, pp. 5771–5781, Jun. 2025.
[38] Z. Zhu, C. Q. Jiang, X. Wang, J. Yang, Y. Wang, and K. Song, "Synchronization strategy based on pulse voltage injection for bidirectional wireless power transfer systems," in *IEEE Trans. Ind. Electron.*, Apr. 2025.
[39] F. Xu, S.-C. Wong, and C. K. Tse, "Inductive power transfer system with maximum efficiency tracking control and real-time mutual inductance estimation," *IEEE Trans. Power Electron.*, vol. 37, no. 5, pp. 6156–6167, May. 2022.
[40] S. Jia, C. Chen, P. Liu, and S. Duan, "A digital phase synchronization method for bidirectional inductive power transfer," *IEEE Trans. Ind. Electron.*, vol. 67, no. 8, pp. 6450–6460, Aug. 2020.
[41] S. R. Sanders, J. M. Noworolski, X. Z. Liu, and G. C. Verghese, "Generalized averaging method for power conversion circuits," in *Proc. 21st Annu. IEEE Conf. Power Electron. Specialists*, 1990, pp. 333–340.
[42] A. Forsyth, G. Ward, and S. Mollov, "Extended fundamental frequency analysis of the LCC resonant converter," *IEEE Trans. Power Electron.*, vol. 18, no. 6, pp. 1286–1292, Nov. 2003.
[43] C.-S. Wang, G. Covic, and O. Stielau, "Investigating an LCL load resonant inverter for inductive power transfer applications," *IEEE Trans. Power Electron.*, vol. 19, no. 4, pp. 995–1002, Jul. 2004.
[44] M. Al-Greer, M. Armstrong, M. Ahmeid, and D. Giaouris, "Advances on system identification techniques for DC–DC switch mode power converter applications," *IEEE Trans. Power Electron.*, vol. 34, no. 7, pp. 6973–6990, Jul. 2019.
[45] F. Chen, A. Padilla, P. C. Young, and H. Garnier, "Data-driven modeling of wireless power transfer systems with slowly time-varying parameters," *IEEE Trans. Power Electron.*, vol. 35, no. 11, pp. 12442–12456, Nov. 2020.
[46] F. Chen, P. C. Young, H. Garnier, Q. Deng, and M. K. Kazimierczuk, "Data-driven modeling of wireless power transfer systems with multiple transmitters," *IEEE Trans. Power Electron.*, vol. 35, no. 11, pp. 11363–11379, Nov. 2020.
[47] F. Chen, H. Hu, L. Zhao, A. Padilla, and J. Hou, "A linear parameter-varying hammerstein model for dynamic modeling of WPT systems," *IEEE Trans. Power Electron.*, vol. 38, no. 12, pp. 16230–16244, Dec. 2023.

Fengwei Chen was born in Chongqing, China. He received the B.Eng. degree in automation and the M.Eng. degree in control theory and control engineering from Wuhan University, Wuhan, China, in 2009 and 2011, respectively, and the Ph.D. degree in automatic control from the Université de Lorraine, Nancy, France, in 2014.

From 2015 to 2016, he was a Lecturer with the Dalian University of Technology, Dalian, China. From 2017 to 2020, he was an Associate Researcher with Wuhan University. Since 2021, he has been with Chongqing University, Chongqing, China, where he is currently an Associate Professor. His research interests include system identification and parameter estimation, with applications to wireless power transfer.

Chanzhen Duan was born in Hubei, China. He received the B.Eng. degree in electrical engineering and automation from the Wuhan Institute of Technology, Wuhan, China, in 2022. He is currently working toward the M.Eng. degree in control engineering with the School of Automation, Chongqing University, Chongqing, China.

His research interests include data-based modeling and control of wireless power transmission systems.

Zhenxing Xu was born in Shandong, China. He received the B.Eng. degree in automation from Sichuan University, Chengdu, China, in 2023. He is currently working toward the M.Eng. degree in control engineering with the School of Automation, Chongqing University, Chongqing, China.

His research focuses on wireless power transfer.

Danli Chen was born in Hubei, China. She received the B.Eng. degree in automation from the Wuhan University of Science and Technology, Wuhan, China, in 2022. She is currently working toward the Ph.D. degree in control science and engineering with the School of Automation, Chongqing University, Chongqing, China.

Her research interests include modeling and control of wireless power transfer systems.

Lei Zhao received the B.S. degree from the Xi'an University of Technology, Xi'an, China, in 2011, and the M.E. degree from The University of Auckland, Auckland, New Zealand, in 2013, both in electrical engineering, and the Ph.D. degree in electrical and electronic engineering from The University of Auckland, in 2019.

From 2019 to 2021, he was a Research Fellow with the Department of Electrical, Computer, and Software Engineering, The University of Auckland, with Prof. A. P. Hu. In 2022, he was with the School of Automation, Chongqing University, Chongqing, China, where he is currently an Associate Professor. His research interests include bidirectional hybrid inductive power transfer systems for electrical vehicle charging and high-frequency power electronics.

Jie Hou received the B.Eng. degree in automation from North Minzu University, Yinchuan, China, in 2010, the M.Eng. degree in control science and engineering from Chongqing University, Chongqing, China, in 2013, and the Ph.D. degree in control theory and control engineering from the Dalian University of Technology, Dalian, China, in 2018.

From 2018 to 2021, he was a Lecturer with the Chongqing University of Posts and Telecommunications, Chongqing, China, where he is currently an Associate Professor. His research interests include system identification and modeling.

Udaya K. Madawala received the B.Sc. (hons.) degree in electrical engineering from the University of Moratuwa, Moratuwa, Sri Lanka, in 1987, and the Ph.D. degree in power electronics from the University of Auckland, Auckland, New Zealand, in 1993, as a Commonwealth Doctoral Scholar.

He is currently a Full Professor. His research interests include power electronics, wireless power transfer, renewable energy, permanent magnet motor drives, and vehicle-to-grid applications.

Dr. Madawala is a Distinguished Lecturer of the IEEE Industrial Electronic Society. He was with IEEE Power Electronics and Industrial Electronics Societies in numerous roles, relating to editorial, advisory, conferences, administrative and technical committees, and chapter activities.